Journal of Membrane Science 640 (2021) 119766

Contents lists available at ScienceDirect

Journal of Membrane Science

journal homepage: www.elsevier.com/locate/memsci

FIB-SEM tomography reveals the nanoscale 3D morphology of virus removal filters

Kaitlyn P. Brickey [a], Andrew L. Zydney [a,*], Enrique D. Gomez [a,b,c,**]

[a] Department of Chemical Engineering, The Pennsylvania State University, University Park, PA, 16802, USA
[b] Department of Materials Science and Engineering, The Pennsylvania State University, University Park, PA, 16802, USA
[c] Materials Research Institute, The Pennsylvania State University, University Park, PA, 16802, USA

ARTICLE INFO

Keywords:
Virus removal filter
Pore morphology
Particle capture
Pore network
FIB-SEM tomography

ABSTRACT

Virus removal filters are designed to ensure very high levels of removal of viruses and virus-like particles during bioprocessing, but the performance of some virus removal filters can be compromised at high-throughputs, after process disruptions, or during operation at low pressures. Several studies have hypothesized that the different behavior is due to differences in underlying pore morphology, but current techniques are limited to examining the 2D pore structure. Here, we use the combination of a focused ion beam and scanning electron microscopy (FIB-SEM) to obtain 3D reconstructions of the pore structure of the asymmetric Viresolve® Pro virus removal filter. Images were obtained through a 3 μm section into the membrane starting at the size-selective skin. The membrane porosity decreases from 41 to 17% as one approaches the filter exit. Model simulations based on flow through the full 3D pore reconstruction show 100% virus retention, with all virus particles captured at least 400 nm from the filter exit. A pore-network model was developed from the reconstructions and used to evaluate the body and throat size distribution and pore interconnectivity. The number of throats is approximately twice the number of bodies, with an average throat size of 21 nm within the selective skin. The pore interconnectivity remains relatively constant at a value of 4 throats per body. These results provide insights into the underlying pore structure of the Viresolve® Pro virus removal filter as well as a general framework for characterizing the 3D pore space in nanoporous membranes.

1. Introduction

Virus filtration is an important component of the overall viral clearance strategy to ensure the removal of viruses and virus-like particles in biopharmaceutical processing [1]. Virus filtration membranes are designed to provide at least 99.9% removal of small (20 nm) virus particles while allowing high transmission of a therapeutic product, e.g., monoclonal antibodies that are approximately 10 nm in size. Virus filtration is thus one of the more highly selective size-based membrane separations with widespread commercial application [2].

It is well established that virus retention for some (but not all) virus removal filters can be compromised under specific operating conditions including after high throughput (large volume) filtration processes [3], during operation at low pressures [4], and after process disruptions [5–7]. Jackson et al. [8] hypothesized that the loss in virus retention at high throughput was due to the accumulation of mobile virus within the porous structure of the DV20 virus removal filter. Woods and Zydney [5] proposed that the increase in virus transmission after a process disruption was due to lateral virus diffusion, with previously captured viruses diffusing through the pore structure and then migrating deeper into, and potentially all the way through, the filter when the filtration was restarted. The presence of virus migration was confirmed by confocal microscopy [5]. Several studies have suggested that virus diffusion also plays a role in the loss of virus retention at low pressures/fluxes in the hollow fiber Planova 20 N filter, with the viruses able to diffuse around potential constrictions within the pore structure [3,6].

In order to understand the connection between virus removal filter performance and the underlying pore morphology, there has been considerable interest in obtaining direct measurements of the pore size and structure of virus filtration membranes using electron microscopy (EM) [9]. Calvo et al. [10] estimated the pore size distribution of nanoporous ultrafiltration membranes using field emission scanning

---

* Corresponding author.,

** Corresponding author. Department of Chemical Engineering, The Pennsylvania State University, University Park, PA, 16802, USA.
E-mail addresses: alz3@psu.edu (A.L. Zydney), edg12@psu.edu (E.D. Gomez).

https://doi.org/10.1016/j.memsci.2021.119766
Received 17 April 2021; Received in revised form 17 August 2021; Accepted 19 August 2021

electron microscopy (FESEM) with results that were found to be in good agreement with liquid-liquid porosimetry data. Nazem-Bokaee et al. [11] visualized the location of virus capture using gold nanoparticles as proxies, with different virus removal filters showing virus capture at very different locations within the depth of the filter. Additionally, protein fouling was shown to shift the location of particle capture further upstream (away from the skin) in some flat-sheet virus removal filters [12]. Adan-Kubo et al. [13] evaluated the pore size gradient through the depth of hollow fiber Planova 15 N and 20 N virus removal filters using transmission electron microscopy (TEM), with results presented in terms of the pore diameter ratio due to limitations of the 2D image analysis of the filter cross-section. None of these studies have provided information on the 3D pore structure of virus filtration membranes.

Three-dimensional reconstructions of membrane pore structures have been developed using advanced scanning or transmission EM techniques [14–17]. Scanning transmission electron tomography has been used to characterize the void structure and polymer density within dense reverse osmosis (RO) membranes [16,18], and focused ion beam-scanning electron tomography (FIB-SEM tomography or FIB-ET) has been used to visualize the pores within polyelectrolyte fuel cell membranes (PEMs) [17], defects in block copolymers [19], and the microporous layers on gas diffusion membranes [20]. The advantages of FIB-SEM compared to freeze-fracturing for imaging organic and inorganic membranes was demonstrated by Qin et al. [21]. The focused ion beam precisely removes sections of the membrane sample with controlled thickness, allowing SEM images to be generated in slices through the depth of the membrane. The resulting 2D images are then binarized and stitched together to obtain a full 3D reconstruction of the pore structure. Klosowski et al. [16] showed that FIB-SEM tomography provided finer surface resolution of RO membranes compared to atomic force microscopy (AFM), where AFM underestimated surface area and the complexity of the polyamide active layer. In the case of PEMs, FIB-SEM tomography allowed the identification and quantification of pore size, porosity, and oxygen diffusivities of the homogenous transition region at the interface between the microporous and catalyst layers. An asymmetric porous ultrafiltration membrane was studied with FIB-SEM tomography, which allowed for visualization of the pore connectivity [15]. More recently, FIB-SEM tomography was used in combination with X-ray tomography to evaluate the structure of PVDF nanofiber membranes, enabling modeling of airflow through the material [22]. 3D reconstructions extracted from FIB-SEM tomography have been used in the modeling of localized transport phenomena that govern membrane performance in a variety of applications [23,24].

Here, we use FIB-SEM tomography to evaluate the morphology of the asymmetric Viresolve® Pro virus removal filter, providing insights into the 3D pore structure of this class of nanoporous membranes. The resulting images were analyzed using GeoDict to evaluate both the membrane permeability and the virus retention characteristics. Avizo was used to generate a pore-network model. These results provide detailed information on the variation in pore size, porosity, and interconnectivity through the depth of the highly retentive nanoporous layer that controls the selectivity of these important virus filtration membranes. The utilization of FIB-SEM tomography to understand the filter pore structure and its relationship to filter performance provides a framework for future development of improved virus removal filters.

2. Materials and methods

2.1. Membrane preparation

Viresolve® Pro virus removal filters were obtained from MilliporeSigma (Burlington, MA) as roll-stock, cut into 5 × 5 mm squares, and fixed onto an SEM stub using conductive tape with the skin layer facing upwards (away from the stub). Samples were coated with 8 nm of iridium prior to placing in the SEM chamber to avoid charging effects.

2.2. FIB-SEM tomography

Imaging was performed using a dual-beam FEI Helios 660 FIB-SEM in the Materials Research Institute at Penn State. Once inside the SEM chamber, a platinum protective layer was deposited by electron beam-induced deposition (EBID) to a height of roughly 10 nm. Fiducial markers were placed near the area of interest using a combination of EBID and ion-beam milling; these were used for image alignment post-acquisition. To carry out the FIB-SEM tomography, the sample was tilted at an angle of 52^{o} so that milling would occur perpendicular to the skin layer. SEM micrographs were collected at an accelerating voltage of 3 kV and beam current of 100 pA using a through-lens detector (TLD) that collected secondary electrons (SE) to limit any pore-back effects [25]. FIB milling was performed at an accelerating voltage of 30 kV and a current between 40 and 79 pA to obtain a 3 nm slice thickness. Some imaging/milling was performed under cryogenic conditions (temperature of less than $-80\ ^{o}C$) to further minimize beam damage. Total image collection time ranged from 2 to 4 h.

2.3. Image and data analysis

After serial image acquisition, Avizo (Thermo Scientific) was used for image analysis including tilt correction, image alignment, grayscale adjustment for slice brightness variation, and binarization. Careful consideration was taken when selecting the threshold value for determination of pore space versus polymer space. Several different thresholds were selected, and the optimal threshold was chosen based on the simulated water flux evaluated in GeoDict as discussed subsequently. An example cross section at different thresholds is shown in Figure S1. The resulting 3D microstructure was then used to evaluate the pore volume fraction and to develop the body/throat pore-network model.

2.4. Simulation of water flux and gold nanoparticle filtration

The water flux through the 3D reconstruction was evaluated using the FlowDict module in GeoDict (Math2Market, Germany) by solution of the Stokes flow equations at a transmembrane pressure drop of 210 kPa (30 psi), which is the typical operating pressure for the Viresolve® Pro filter. The calculated volumetric flow rate was normalized by the membrane area and operating pressure to evaluate the permeability in units of $L\ m^{-2}\ h^{-1}\ psi^{-1}$ (LMH/psi). Gold nanoparticle capture was simulated using the FilterDict-Media solver at the same pressure. 20 nm nanoparticles were added to the feed at the membrane inlet at a concentration of 10^{8} particles mL^{-1}. Particle transport through the 3D reconstruction accounted for particle-particle and particle-wall collisions as well as Brownian diffusion. Nanoparticle capture occurred whenever the diameter of the particle was equal to or larger than that of the pathway accounting for the actual three-dimensional structure of the pore space.

2.5. Generation of pore-network model

A pore-network model was developed using the pore network modeling extension in Avizo, with the pore space represented as a series of larger spheres (bodies) connected by narrow cylinders (throats). The module graphs watershed lines on a Euclidian distance map of the 3D volume, separating individual pore pathways from one another. Bodies and throats are identified based on local minima within the structure. Coordinates that represent the distance from the skin layer (with 0 nm considered to be the edge of the skin layer at the filter exit) were taken to be the center of the spherical bodies and, for throats, assigned the coordinate of its first connected pore.

3. Results and discussion

Two separate reconstructions, one at room-temperature (25 °C) and one at cryogenic temperature (−80 °C), were obtained for the Viresolve® Pro virus removal filter using membrane samples cut from different locations on the same flat sheet. For the larger data set, a total of 407 serial images were acquired at 3 nm slice increments. One of the unprocessed micrographs and the associated binarized images at different threshold values are provided in Figure S1. The best threshold value (Fig. S1 (C)) was chosen so that the simulated permeability through the resulting 3D reconstruction most closely matched that reported previously for a single layer of the Viresolve® Pro filter (1250 LMH at 30 psi, or ~40 LMH/psi) [12]. This analysis neglects the hydraulic resistance provided by the rest of the Viresolve® Pro membrane, which is likely to provide only a small contribution to the overall permeability due to the rapidly increasing pore size [11]. Reconstructions that were below the optimal threshold value/permeability were missing some of the smaller connecting pathways, while reconstructions above that value showed significant "noise" that appears as false connections.

The optimized reconstruction for one of the samples, with 2.7 × 3.0 × 1.2 μm total image volume, is shown in Fig. 1, and a high-resolution view is shown in Figure S2. The asymmetric structure of the filter is readily visible even over this 3 μm thick region, with the pore size increasing as one moves away from the filter exit (skin layer) and into the depth of the membrane. Some voids as small as 3 nm in diameter were visible in the region close to the skin layer in the reconstructions for both samples. Additionally, there were no major observable differences between reconstructions that were obtained at cryogenic conditions (denoted as "Cryo" in Figs. 3, 5 and 6) versus room temperature (denoted as "RT" in Figs. 3, 5 and 6). The porosity evaluated from the image of the cryogenic sample was found to be slightly higher than that for the room temperature sample (Fig. 3). These differences are likely due to inherent experiment-to-experiment variability in image acquisition and between samples, although it is possible that the room-temperature and cryogenic FIB-SEM acquisitions lead to small differences in the visualized pore space. Additional comparison of the results obtained during imaging at room temperature and under cryogenic conditions is discussed below.

In addition to simulating the permeability, we also used GeoDict to confirm that the 3D reconstructions have the appropriate virus retention characteristics. In this case the 3D reconstructions were challenged with a feed containing 20 nm non-interacting particles at a concentration of 10^8 particles mL^{-1} and a transmembrane pressure of 210 kPa (30 psi), giving a total of 971 particles over the simulated filtration experiment. We expect the final particle location of the 20 nm particles to agree most closely with results obtained by Nazem-Bokaee [11] and others [26,27] that have used gold nanoparticles as a model to study virus retention and capture. These studies have demonstrated that the gold nanoparticles have similar retention characteristics and capture locations as bacterial and mammalian viruses even though the gold has different electrostatic interactions and surface roughness than actual viruses. The final capture location of each particle for the room temperature reconstruction is shown in Fig. 2; results for the cryogenic reconstruction look nearly identical. The particles appear to form clusters in specific "hot spots" for virus capture, in good agreement with SEM images of gold nanoparticles captured within the Viresolve® Pro filter [11]. All of the particles in the feed are captured by the filter, corresponding to a log removal value ≥ 2.9, consistent with the reported 3–4 log virus removal by a single layer of the Viresolve® Pro membrane [28]. The furthest nanoparticle traveled to a final location roughly 400 nm away from the skin (filter exit), compared to experimental results with gold nanoparticles showing a closest approach of around 200 nm [11]. The gold nanoparticles used by Nazem-Bokaee et al., however, varied in size from about 11 to 50 nm. Thus, the nanoparticles that were captured within 200 nm of the filter exit may well have been considerably smaller than the uniform 20 nm particles used in these simulations.

The 3D reconstructions of the Viresolve® Pro filter were also used to evaluate the porosity of the membrane as a function of distance over the 3 μm thickness of the sample. Results are shown in Fig. 3 for the two reconstructions taken at different temperatures, with the void volume determined over 6 separate slices, each 500 nm thick, beginning at the

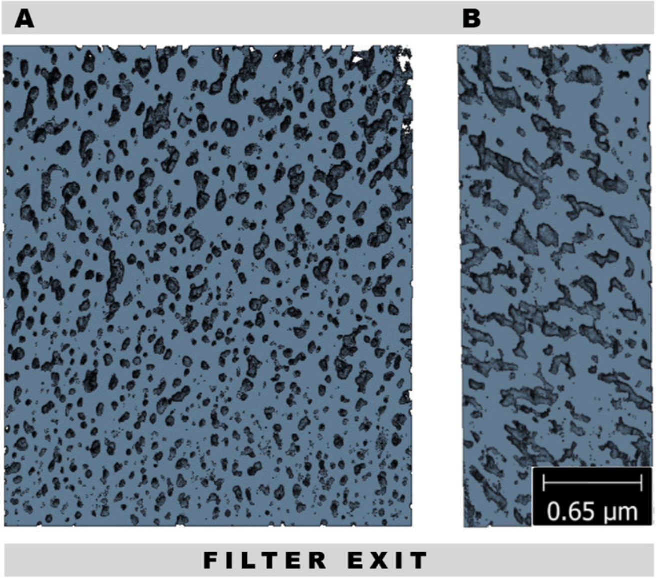

Fig. 1. Cross section (A) and edge on view (B) from a 3D reconstruction of a Viresolve® Pro membrane obtained from serial sectioning using cryogenic FIB-SEM. Grey structure depicts polymer region.

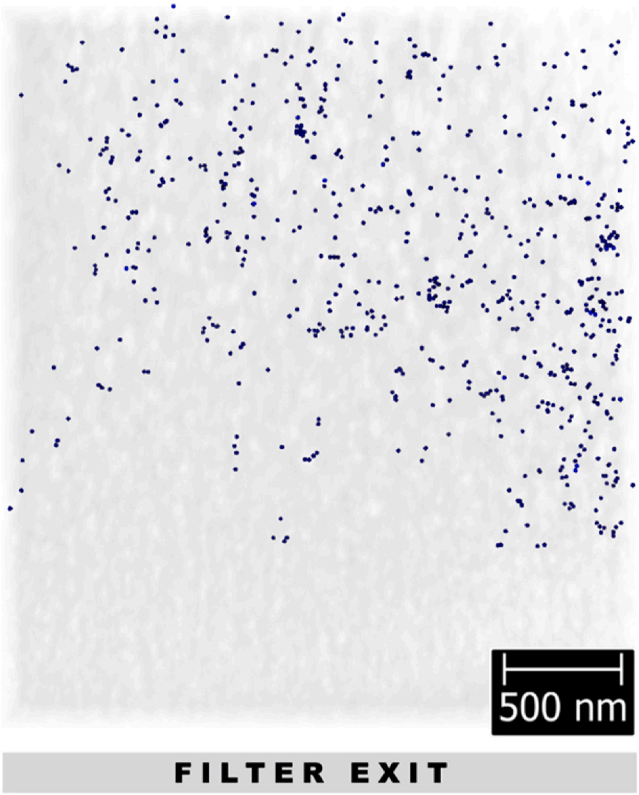

Fig. 2. Simulations of particle capture within the reconstruction of the Viresolve® Pro membrane obtained using room temperature FIB-SEM tomography. Filter was challenged with 20 nm non-interacting particles at a concentration of 10^8 particles/mL using GeoDict software. Direction of flow is such that the filter skin is located at the bottom of the reconstruction. 20 nm nanoparticles are shown as blue spheres. Polymer is depicted as transparent grey.

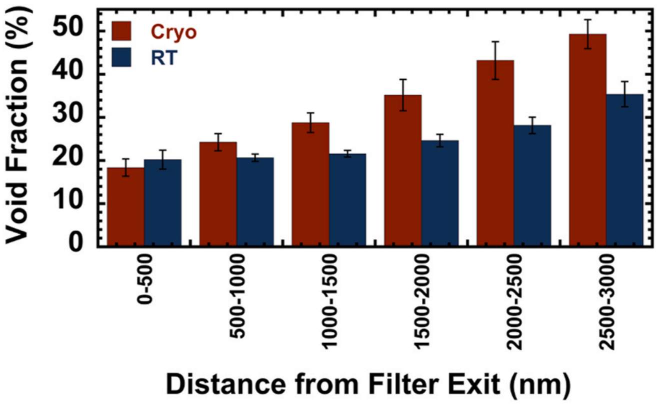

Fig. 3. Percent void fraction within the Viresolve® Pro membranes extracted from FIB-SEM tomographs obtained at cryogenic (Cryo) and room temperature (RT). Error bars represent standard deviation.

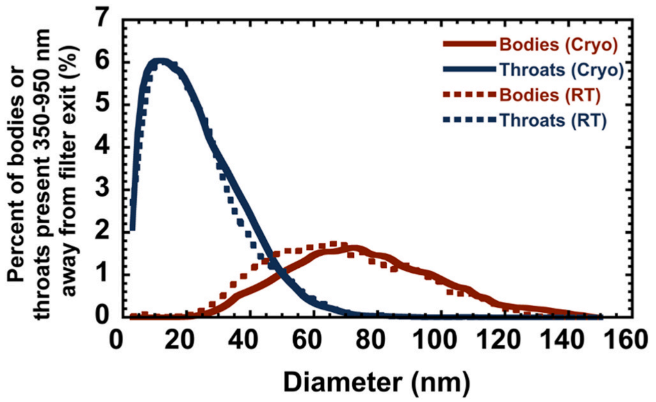

Fig. 5. Number size distributions of the bodies (red lines) and throats (blue lines) near the skin layer extracted from 3D reconstructions for a Viresolve® Pro membrane using cryogenic (solid, Cryo) and room temperature (dashed, RT) FIB-SEM tomography in the area previously identified for primary virus capture (350–950 nm away from the filter exit). (For interpretation of the references to colour in this figure legend, the reader is referred to the Web version of this article.)

filter exit (skin) and moving into the depth of the membrane. The volume fraction is smallest in the slice closest to the filter exit (approximately 18% for both samples), increasing with position as one moves deeper into the filter. The increase in void fraction is steeper for the cryogenic sample compared to the one obtained at room temperature, where the final void fraction (about 3000 nm into the filter exit) is 49% compared to 36%, respectively. This may be due to the inherent variability between samples. Only 0.2% of the total void volume are inaccessible voids, *i.e.*, pore space that is totally unconnected to either the inlet or outlet surfaces of the reconstruction.

In order to quantify the properties of the membrane microstructure, a simple pore-network model was developed to represent the void space (Fig. 4, S3, S4) as a series of bodies and throats. Pore-network models have previously been used to describe the void space in porous electrodes [29] and porous rock formations associated with oil recovery [29–31]. Fig. 4 shows the body-throat representation for the Viresolve® Pro filter reconstruction from Fig. 1 (at the same length scale) with the bodies shown as red spheres and the throats as blue cylinders. Fig. 4C shows a small section of the pore network model located just upstream of the filter exit. Many of the bodies seen in Fig. 4 are not visible in the frontal slice in Fig. 1 since they are located beyond the exterior plane of the reconstruction. The calculated porosity for the pore-network model is 25.2%, which agrees with the 25.4% porosity determined directly from the FIB-SEM reconstruction.

The average size of both the bodies and throats decreases in the region closer to the filter exit (top to bottom of the panel in Fig. 4A). For example, the average size of the bodies in the 500 nm region furthest from the exit is 103 ± 43 nm, while the average body size in the 500 nm region closest to the filter exit is 69 ± 28 nm. The corresponding values for the throats are 39 ± 27 nm and 19 ± 12 nm where the plus/minus represents the standard deviation.

The number distributions for both the body and throat size in a slice through the Viresolve® Pro virus removal filter located between 350

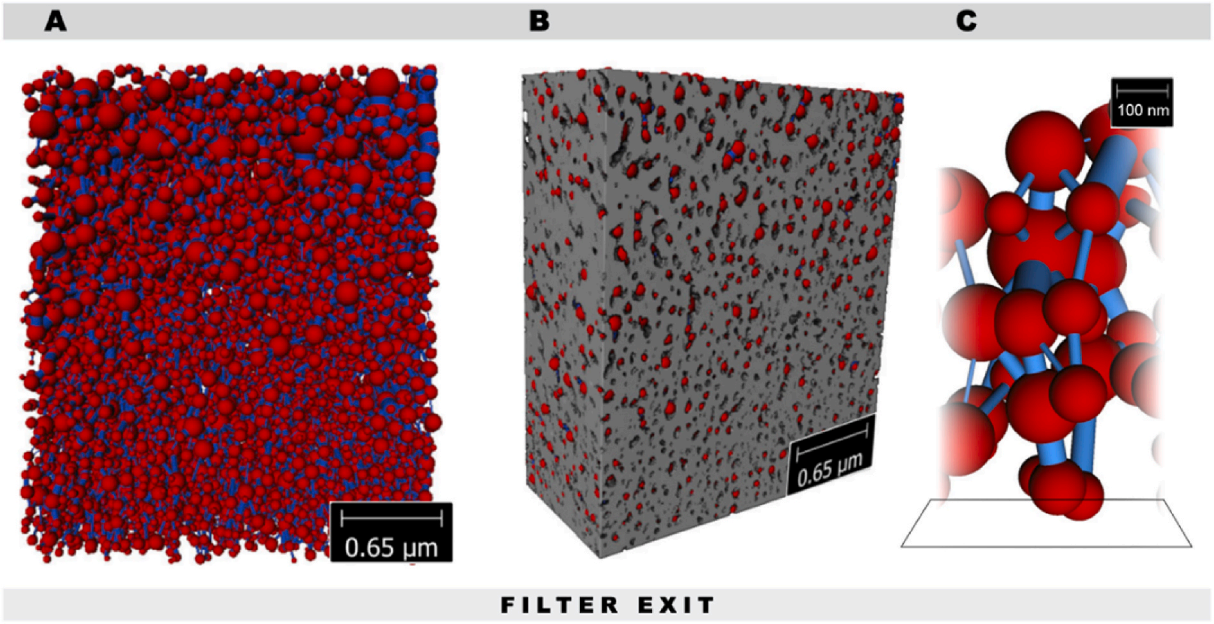

Fig. 4. (A) Pore network model generated from the 3D reconstruction of a Viresolve® Pro membrane shown in Fig. 1. The void space within the membrane is represented as a series of interconnected bodies and throats. Red depicts bodies and blue depicts restrictive throats. (B) Inlay of pore network model within the 3D reconstruction. (C) High magnification illustration of the pore network model connectivity located at the filter exit (indicated by black rectangle at lower right of inlay). (For interpretation of the references to colour in this figure legend, the reader is referred to the Web version of this article.)

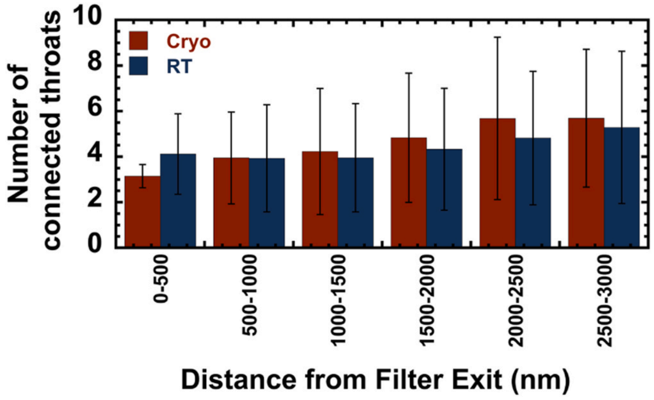

Fig. 6. Pore connectivity for the Viresolve® Pro membrane obtained from the pore network model using micrographs collected at cryogenic (Cryo) and room (RT) temperatures. Error bars represent standard deviation for all pores in each binned region.

and 950 nm in from the skin is shown in Fig. 5; this is the region that has previously been identified as the primary location for virus capture based on SEM images of captured gold nanoparticles [11]. Results are shown for a sample examined at room temperature and one examined under cryogenic conditions; the size distributions for these two samples are nearly indistinguishable, providing further indication that the ion beam milling caused no significant alteration to the pore structure. A total of 2582 throats and 1234 bodies are present in this region between both samples. The throats range in size from 2 to 107 nm, with mean of 21 nm and a standard deviation of 14 nm. The bodies range from 24 to 176 nm with mean of 73 nm and standard deviation of 23 nm. Previous analyses of the pore size variation through the depth of the Viresolve® Pro filter (obtained from SEM images of a cross-section through the depth of the membrane) reported an average pore size of about 18 nm just beneath the skin [11], which is in good agreement with our mean size determined for the throats. The previous 2D analysis does not capture the much larger size of the bodies in the network model, although the pores observed in a 2D slice will always appear smaller than the actual pore size because much of the observed void volume will be seen at angles that pass obliquely through the "edge" of the pores.

The pore network model was also used to calculate the pore interconnectivity, defined as the number of throats connected to each body within the network as shown in Fig. 4C. Unconnected bodies have an interconnectivity of zero throats per body, edge and dead-end pores have a connectivity of at least 1 throat per body, and all other pores have a connectivity of at least 2 throats per body (an inlet and outlet). Most of the bodies in Fig. 4C have multiple throat connections where the throats are all oriented in a largely vertical direction, i.e., in the direction of the filtration flow through the membrane, and appear to be highly interconnected in 3D space. Interconnectivity data was binned in 500 nm increments, similarly to the approach used to evaluate the porosity in Fig. 3. The calculated values of the interconnectivity for the two samples (Fig. 6) are very similar, and increase slightly as one moves deeper into the filter (away from the size-selective skin). The average interconnectivity over the 3 μm region is approximately four, suggesting that on average each body is "fed" by 2 throats and has 2 distinct exit pathways. This idealized body configuration of 2 inlets and 2 outlets is consistent with the high degree of interconnectivity reported previously by Fallahianbijan et al. based on nanoparticle capture profiles in Viresolve® Pro membranes in which a portion of the filter exit was intentionally blocked [32]. This high interconnectivity should provide some protection against membrane fouling since the bodies will remain largely accessible to flow even when one of the throats entering/exiting the body becomes blocked. The interconnectivity does appear to decrease slightly as one moves towards the filter exit. The implications of this for virus removal filter performance are beyond the scope of the current study, but the presented pore-network model provides a framework for evaluating the pore connectivity of virus removal filters, potentially yielding insights into the relationship between pore morphology and key performance metrics, e.g., filter capacity, virus removal efficiency, and product transmission and yield.

For example, in nanoscale pore clusters within shale gas reservoirs, the use of a pore-network model developed from 3D FIB-SEM images highlighted the importance of the throat flux-radius distribution on the gas recoverability [24]. Additionally, this type of pore-network model could be used to study the local transport phenomena in other ultrafiltration and nanoporous membranes. Meybodi et al. [33] examined the flow through a variety of body-throat model structures to develop a better understanding of polymer transport and trapping in porous rocks. The same methodology could be applied to study the performance of virus filtration/ultrafiltration membranes with FIB-SEM enabling the quantification of the body and throat diameters. With future improvements in 3D printing, a realistic microfluidic model could also be designed using reconstructions from FIB-SEM tomography, allowing for real-time visualization of membrane fouling and nanoparticle capture.

4. Conclusions

Virus removal filters play a critical role in ensuring the safety of biopharmaceutical products, but there is currently little understanding of the relationship between the underlying pore structure and the performance characteristics of these membranes. This study used FIB-SEM tomography to obtain a detailed 3D reconstruction for the pore structure of the Viresolve® Pro membrane in the 3 μm region nearest the filter exit, which is known to be the size-selective region associated with virus capture. Our 3D reconstructions find that only 0.2% of the void volume is "inaccessible" to the external surface of the filter. While this inaccessible void volume is negligible within the Viresolve® Pro membrane, this may not be true for other virus or ultrafiltration membranes.

The hydraulic permeability of the reconstructed membrane was evaluated directly from solution of the Stokes flow equations through the detailed pore geometry using GeoDict. The calculated value of 40 LMH/psi is in good agreement with previously reported values [12]. In addition, simulations show that the reconstructed membrane has >99.8% retention of 20 nm particles, with these particles captured in the region between 400 and 1500 nm upstream of the filter exit, both of which are in good agreement with experimental observations for both gold nanoparticles and model viruses. These results provide strong evidence that the 3D reconstruction provides an accurate picture of the detailed pore space in the size-selective region of the Viresolve® Pro membrane. Furthermore, the simulations of virus capture in the 3D pore reconstructions can be used to explore the detailed morphology of the pore regions that dominate virus capture, thereby aiding efforts to design future membranes with enhanced virus removal filtration performance. Regions of fouling within virus removal filters and other filtration membranes could also be studied using 3D images obtained from FIB-SEM.

The largest reconstruction consisted of 407 image cross-sections with 3 nm slice (depth) resolution based on milling through the filter. This volume was used to generate a pore network model consisting of spherical bodies connected by one or more restrictive throats. The bodies and throats both have broad size distributions, with the mean size increasing with distance from the size-selective skin. The mean size of the throats near the filter exit is 21 nm, in good agreement with previous SEM images and with the expected size based on the high retention of 20 nm viruses by the Viresolve® Pro filter. The pore network model was then used to evaluate the pore interconnectivity based on the average number of throats per body. The pore connectivity is relatively constant throughout the 3 μm region near the selective skin, with an average of 4 throats per body. Previous studies have suggested that differences in pore connectivity can explain the observed differences in virus removal filter performance [32].

The FIB-SEM methodology developed in this study should provide a general approach that can be used to characterize the full 3D pore structure, and, in turn, key performance characteristics, of different virus removal and ultrafiltration membranes. For example, while the work herein focused on morphological characterization of the pore space, 3D reconstructions of virus removal filter structures have been used by Culp et al. [18] to evaluate the effective diffusion coefficient of water in these nanoporous membranes. The combination of FIB-SEM and a network model has also been successfully used to evaluate model parameters for describing dextran adsorption in microfiltration membranes [23]. Future studies will be required to develop a quantitative understanding of the connection between the measured pore connectivity (based on the pore network model) and the detailed 3D distribution of the void volume (determined directly from the FIB-SEM reconstructions) on the key performance characteristics of these virus removal filtration membranes.

CRediT authorship contribution statement

Kaitlyn P. Brickey: Methodology, Validation, Formal analysis, Investigation, Data curation, Writing – original draft, Writing – review & editing, Visualization. **Andrew L. Zydney:** Conceptualization, Methodology, Resources, Writing – review & editing, Supervision, Project administration, Funding acquisition. **Enrique D. Gomez:** Conceptualization, Methodology, Writing – review & editing, Supervision, Project administration, Funding acquisition.

Declaration of competing interest

The authors declare that they have no known competing financial interests or personal relationships that could have appeared to influence the work reported in this paper.

Acknowledgements

The authors would like to thank Trevor Clark from the Materials Research Institute at Penn State for instrument support, Bryce Allison for assistance with data analysis, and Sal Giglia and Christina Carbrello at MilliporeSigma for useful technical discussions. This work was supported through the Membrane Science, Engineering, and Technology (MAST) Center, which is funded by grant number 1841474 from the U.S. NSF IUCRC program.

Appendix A. Supplementary data

Supplementary data to this article can be found online at https://doi.org/10.1016/j.memsci.2021.119766.

References

[1] R. Van Reis, A. Zydney, Bioprocess membrane technology, J. Membr. Sci. 297 (2007) 16–50.
[2] M. Billups, M. Minervini, M. Holstein, H. Feroz, S. Ranjan, J. Hung, H. Bao, S. Ghose, Z.J. Li, A.L. Zydney, Antibody retention by virus filtration membranes: polarization and sieving effects, J. Membr. Sci. 620 (2021) 118884.
[3] S. Lute, M. Bailey, J. Combs, M. Sukumar, K. Brorson, Phage passage after extended processing in small-virus-retentive filters, Biotechnol. Appl. Biochem. 47 (2007) 141.
[4] D. Strauss, J. Goldstein, T. Hongo-Hirasaki, Y. Yokoyama, N. Hirotomi, T. Miyabayashi, D. Vacante, Characterizing the impact of pressure on virus filtration processes and establishing design spaces to ensure effective parvovirus removal, Biotechnol. Prog. 33 (2017) 1294–1302.
[5] M.A. Woods, A.L. Zydney, Effects of a pressure release on virus retention with the Ultipor DV20 membrane, Biotechnol. Bioeng. 111 (2014) 545–551.
[6] D. LaCasse, P. Genest, K. Pizzelli, P. Greenhalgh, L. Mullin, A. Slocum, Impact of process interuption on virus retention of small-virus filters, in: BioProcess International, 2013, pp. 34–44.
[7] D. Lacasse, S. Lute, M. Fiadeiro, J. Basha, M. Stork, K. Brorson, R. Godavarti, C. Gallo, Mechanistic failure mode investigation and resolution of parvovirus retentive filters, Biotechnol. Prog. 32 (2016) 959–970.
[8] N.B. Jackson, M. Bakhshayeshi, A.L. Zydney, A. Mehta, R. Van Reis, R. Kuriyel, Internal virus polarization model for virus retention by the Ultipor®VF Grade DV20 membrane, Biotechnol. Prog. 30 (2014) 856–863.
[9] Y. Hamamoto, S. Harada, S. Kobayashi, K. Yamaguchi, H. Iijima, S.-I. Manabe, T. Tsurumi, H. Aizawa, N. Yamamoto, A novel method for removal of human immunodeficiency virus: filtration with porous polymeric membranes, Vox Sang. 56 (1989) 230–236.
[10] J.I. Calvo, R.I. Peinador, P. Prádanos, A. Bottino, A. Comite, R. Firpo, A. Hernández, Porosimetric characterization of polysulfone ultrafiltration membranes by image analysis and liquid–liquid displacement technique, Desalination 357 (2015) 84–92.
[11] H. Nazem-Bokaee, F. Fallahianbijan, D. Chen, S.M. O'Donnell, C. Carbrello, S. Giglia, D. Bell, A.L. Zydney, Probing pore structure of virus filters using scanning electron microscopy with gold nanoparticles, J. Membr. Sci. 552 (2018) 144–152.
[12] F. Fallahianbijan, S. Giglia, C. Carbrello, D. Bell, A.L. Zydney, Impact of protein fouling on nanoparticle capture within the Viresolve® Pro and Viresolve® NFP virus removal membranes, Biotechnol. Bioeng. 116 (2019) 2285–2291.
[13] J. Adan-Kubo, M. Tsujikawa, K. Takahashi, T. Hongo-Hirasaki, K. Sakai, Microscopic visualization of virus removal by dedicated filters used in biopharmaceutical processing: impact of membrane structure and localization of captured virus particles, Biotechnol. Prog. 35 (2019), e2875.
[14] T.E. Culp, Y.-X. Shen, M. Geitner, M. Paul, A. Roy, M.J. Behr, S. Rosenberg, J. Gu, M. Kumar, E.D. Gomez, Electron tomography reveals details of the internal microstructure of desalination membranes, Proc. Natl. Acad. Sci. USA 115 (2018) 8694–8699.
[15] G. Sundaramoorthi, M. Hadwiger, M. Ben-Romdhane, A.R. Behzad, P. Madhavan, S.P. Nunes, 3D membrane imaging and porosity visualization, Ind. Eng. Chem. Res. 55 (2016) 3689–3695.
[16] M.M. Kłosowski, C.M. Mcgilvery, Y. Li, P. Abellan, Q. Ramasse, J.T. Cabral, A. G. Livingston, A.E. Porter, Micro-to nano-scale characterisation of polyamide structures of the SW30HR RO membrane using advanced electron microscopy and stain tracers, J. Membr. Sci. 520 (2016) 465–476.
[17] L. Zielke, S. Vierrath, R. Moroni, A. Mondon, R. Zengerle, S. Thiele, Three-dimensional morphology of the interface between micro porous layer and catalyst layer in a polymer electrolyte membrane fuel cell, RSC Adv. 6 (2016) 80700–80705.
[18] T.E. Culp, B. Khara, K.P. Brickey, M. Geitner, T.J. Zimudzi, J.D. Wilbur, S.D. Jons, A. Roy, M. Paul, B. Ganapathysubramanian, A.L. Zydney, M. Kumar, E.D. Gomez, Nanoscale control of internal inhomogeneity enhances water transport in desalination membranes, Science 371 (2021) 72–75.
[19] E. Thomas, X. Feng, W. Shan, Slice and view SEM tomography of 3D periodic block copolymer tubular morpholgies, Microsc. Microanal. 26 (2020) 888–890.
[20] H. Ostadi, P. Rama, Y. Liu, R. Chen, X.X. Zhang, K. Jiang, 3D reconstruction of a gas diffusion layer and a microporous layer, J. Membr. Sci. 351 (2010) 69–74.
[21] L. Qin, I.A. Mergos, H. Verweij, Obtaining accurate cross-section images of supported polymeric and inorganic membrane structures, J. Membr. Sci. 476 (2015) 194–199.
[22] Z. Pan, X. Zhang, Z. Sun, F. Jiang, L. Lin, Y. Liang, M. Tang, J. Wang, High fidelity simulation of ultrafine PM filtration by multiscale fibrous media characterized by a combination of X-ray CT and FIB-SEM, J. Membr. Sci. 620 (2021) 118925.
[23] S.M. Abdoli, S. Shafiei, A. Raoof, A. Ebadi, Y. Jafarzadeh, H. Aslannejad, Water flux reduction in microfiltration membranes: a pore network study, Chem. Eng. Technol. 41 (2018) 1566–1576.
[24] W. Jiang, M. Lin, Z. Yi, H. Li, S. Wu, Parameter determination using 3D FIB-SEM images for development of effective model of shale gas flow in nanoscale pore clusters, Transport Porous Media 117 (2017) 5–25.
[25] M. Andrew, Comparing organic-hosted and intergranular pore networks: topography and topology in grains, gaps and bubbles, Geological Society, London, Special Publications 484 (2020) 241–253.
[26] F. Fallahianbijan, S. Giglia, C. Carbrello, A.L. Zydney, Use of fluorescently-labeled nanoparticles to study pore morphology and virus capture in virus filtration membranes, J. Membr. Sci. 536 (2017) 52–58.
[27] P. Kosiol, M.T. Müller, B. Schneider, B. Hansmann, V. Thom, M. Ulbricht, Determination of pore size gradients of virus filtration membranes using gold nanoparticles and their relation to fouling with protein containing feed streams, J. Membr. Sci. 548 (2018) 598–608.
[28] R. Cameron, K. Smith, Virus clearance methods applied in bioprocessing operations: an overview of selected inactivation and removal methods, Pharmaceutical bioprocessing 2 (2014) 75–83.
[29] L. Zhang, W. Jing, Y. Yang, H. Yang, Y. Guo, H. Sun, J. Zhao, J. Yao, The investigation of permeability calculation using digital core simulation technology, Energies 12 (2019) 3273.
[30] A. Gayon Lombardo, B.A. Simon, O. Taiwo, S.J. Neethling, N.P. Brandon, A pore network model of porous electrodes in electrochemical devices, J. Energy Storage 24 (2019) 100736.
[31] E.G. Martínez-Mendoza, M.A. Díaz-Viera, M. Coronado, A.T. Mendoza-Rosas, Capillary pressure and relative permeability estimation for low salinity waterflooding processes using pore network models, J. Petrol. Sci. Eng. 182 (2019) 106253.
[32] F. Fallahianbijan, S. Giglia, C. Carbrello, A.L. Zydney, Quantitative analysis of internal flow distribution and pore interconnectivity within asymmetric virus filtration membranes, J. Membr. Sci. 595 (2020) 117578.
[33] H. Emami Meybodi, R. Kharrat, M. Nasehi Araghi, Experimental studying of pore morphology and wettability effects on microscopic and macroscopic displacement efficiency of polymer flooding, J. Petrol. Sci. Eng. 78 (2011) 347–363.